Received: 6 May 2021 | Revised: 1 June 2021 | Accepted: 1 June 2021

DOI: 10.1002/dvdy.383

RESEARCH ARTICLE

Developmental Dynamics WILEY

Deletion of *Fibroblast growth factor 9* globally and in skeletal muscle results in enlarged tuberosities at sites of deltoid tendon attachments

Connor C. Leek[1,2] | **Jaclyn M. Soulas**[1,3] | **Iman Bhattacharya**[1,4] | **Elahe Ganji**[1,2] | **Ryan C. Locke**[1] | **Megan C. Smith**[1,5,6] | **Jaysheel D. Bhavsar**[4] | **Shawn W. Polson**[1,4] | **David M. Ornitz**[7] | **Megan L. Killian**[1,2]

[1]College of Engineering, University of Delaware, Newark, Delaware

[2]Department of Orthopaedic Surgery, Michigan Medicine, Ann Arbor, Michigan

[3]College of Agriculture and Natural Resources, University of Delaware, Newark, Delaware

[4]Center for Bioinformatics and Computational Biology, University of Delaware, Newark, Delaware

[5]Department of Biological Sciences, University of Pittsburgh, Pittsburgh, Pennsylvania

[6]Department of Cell Biology, University of Pittsburgh School of Medicine, Pittsburgh, Pennsylvania

[7]Department of Developmental Biology, Washington University School of Medicine, St Louis, Missouri

Correspondence
Megan L. Killian, Department of Orthopaedic Surgery, University of Michigan, Ann Arbor, MI, USA.
Email: mlkillia@umich.edu

Funding information
Division of Civil, Mechanical and Manufacturing Innovation, Grant/Award Number: CAREER 1944448; National Center for Medical Rehabilitation Research, Grant/Award Number: K12HD073945; National Institute of Arthritis and Musculoskeletal and Skin Diseases, Grant/Award Numbers: P30AR069620, P30AR074992; National Institute of Child Health and Human Development, Grant/Award Numbers:

Abstract

Background: The growth of most bony tuberosities, like the deltoid tuberosity (DT), rely on the transmission of muscle forces at the tendon-bone attachment during skeletal growth. Tuberosities distribute muscle forces and provide mechanical leverage at attachment sites for joint stability and mobility. The genetic factors that regulate tuberosity growth remain largely unknown. In mouse embryos with global deletion of *fibroblast growth factor 9* (*Fgf9*), the DT size is notably enlarged. In this study, we explored the tissue-specific regulation of DT size using both global and targeted deletion of *Fgf9*.

Results: We showed that cell hypertrophy and mineralization dynamics of the DT, as well as transcriptional signatures from skeletal muscle but not bone, were influenced by the global loss of *Fgf9*. Loss of *Fgf9* during embryonic growth led to increased chondrocyte hypertrophy and reduced cell proliferation at the DT attachment site. This endured hypertrophy and limited proliferation may explain the abnormal mineralization patterns and locally dysregulated expression of markers of endochondral development in $Fgf9^{null}$ attachments. We then showed that targeted deletion of *Fgf9* in skeletal muscle leads to postnatal enlargement of the DT.

Conclusion: Taken together, we discovered that *Fgf9* may play an influential role in muscle-bone cross-talk during embryonic and postnatal development.

KEYWORDS

bone shape, enthesis, mechanics, muscle, skeleton

Connor C. Leek and Jaclyn M. Soulas shared co-first authorship.

R01HD049808, R03HD094594; National Institute of General Medical Sciences, Grant/Award Numbers: P20GM103446, P30GM103333; University of Delaware Research Foundation

1 | INTRODUCTION

The transmission of muscle forces to bone via tendons is required for the functional growth of the vertebrate skeleton.[1-5] Bone ridges and tuberosities are skeletal "superstructures" that transmit muscle forces to the periosteal surface of long bones and increase leverage at sites of tendon attachments.[4,6-8] The presence of superstructures requires both initiation of a modular *Sox9* +/*Scx* + progenitor cell pool[7] and maintenance of skeletal muscle contraction.[3,4,9-11] One of the most prominent superstructures in the mouse skeleton is the deltoid tuberosity (DT) of the humerus, which is a migratory tendon attachment that projects anterolaterally from the shoulder with a fin-like shape.[12] Migratory tendon attachments are first established by a population of *Sox9* + progenitor cells during embryonic development. Subsequently, these *Sox9*+ cells are then replaced by *Gli1*+ progenitor cells during postnatal growth.[12] As such, the growth of tendon attachments is likened to that of an arrested growth plate,[6,13] with the attachment includes a layered arrangement of hypertrophic and pre-hypertrophic *Gli1*+ cells, similar to the growth plate during endochondral ossification, as well as a mineralized gradient at the enthesis between tendon and bone.[6,8,13]

Because it is a site of tendon attachments, the DT is also a phenotypic readout for estimating muscle loads during embryonic development in mice. For example, in muscular-compromised mouse models ($Myf5^{null}$: $MyoD^{null}$, *Mdg*, and *Spd* mutants), the DT fails to maintain its size and shape during the mid-to-late stages of embryonic growth.[3,4,9-11] Conversely, mice with genetic mutations that lead to increased muscle mass (e.g., $myostatin^{-/-}$ mice) exhibit an autonomous increase in the size and shape of the DT.[14] Though many mutations related to skeletal muscle unloading result in smaller bone ridges,[3,4,9-11] embryos that lack the protein-encoding gene for Fibroblast growth factor 9 (*Fgf9*) have enlarged DTs.[15] Surprisingly, even though the DTs are enlarged, the stylopods (i.e., humeri and femurs) of *Fgf9* mutant ($Fgf9^{null}$) embryos are shorter and experience delayed growth plate hypertrophy and proliferation, as well as reduced angiogenesis, ultimately restricting osteogenesis during long bone development.[15,16] These phenotypic differences between DT growth and long bone development in $Fgf9^{null}$ embryos suggest a unique role of *Fgf9* as a negative regulator of growth in attachment superstructures.

FGF9 is one of three ligands in the fibroblast growth factor (FGF) family known to be involved in bone development.[17-28] In the developing limb, *Fgf9* is expressed as early as embryonic day 10.5 (E10.5) within the apical ectodermal ridge.[15,29-31] As limb development progresses, expression of *Fgf9* coincides with expression of other chondrogenic markers, such as *Fgfr2* and *Fgf18*.[15,32,33] In periosteal and trabecular osteoblasts, overexpression of *Fgf9* leads to smaller mice with shorter growth plates.[26] Although *Fgf9* expression is required for long bone growth, its expression is predominantly found in the surrounding muscle and perichondral cells and not in the bone anlagen, suggesting that FGF9 may also originate from surrounding soft tissues.[15,29,30] However, the role of tissue specific *Fgf9* on the growth of bony superstructures like the DT has not been explored.

In this study, we hypothesized that global knockout of *Fgf9* leads to increased expansion and growth of the arrested growth plate at sites of migratory tendon attachments. We quantified the size of the DT superstructure using whole-mount staining and characterized cell shape and size using histomorphometry. We then used multiplexed fluorescence in situ hybridization (FISH) at key timepoints during embryonic growth to visualized expression of growth plate markers at the tendon attachment of the DT in wild-type and $Fgf9^{null}$ limbs. We used RNA sequencing (RNAseq) to identify differentially expressed genes between WT and $Fgf9^{null}$ bone anlagen and skeletal muscle during late embryonic development. Surprisingly, we found significant differential expression in muscle, but not bone. Therefore, we developed conditional muscle-specific *Fgf9* knockout mice ($Fgf9^{cKO}$) to determine the effect of muscle-specific deletion of *Fgf9* on postnatal DT size and skeletal muscle innervation. Our findings suggest a muscle-specific role of FGF9 in the size of stylopod superstructures, further expanding the role of FGF signaling in musculoskeletal development.

2 | RESULTS

2.1 | Global loss of *Fgf9* results in an enlarged DT, even with a shortened humerus

To confirm the larger size of the DT in $Fgf9^{null}$ neonates suggested previously by Hung et al., we used whole-

mount staining to visualize cartilage with Alcian Blue and mineralized bone with Alizarin Red.[15] We found that *Fgf9*^{null} neonates had a 68% larger ratio of the DT area to total humerus area compared with WT neonates at postnatal day 0 (P0) (Figure 1A,B). The DT was wider and shorter in *Fgf9*^{null} neonates compared with WT littermates. *Fgf9*^{null} neonates also had a similar total humerus area compared with WT neonates (Figure 2B). We did not find a sex-dependent effect of global *Fgf9* deletion on DT size (Figure 1, blue and pink dots).

We observed increased Alcian Blue-stained cartilage on the crest of the DT in *Fgf9*^{null} neonates, but this cartilage was absent on the crest of stage-matched WT DTs (Figure 1A, arrows). In line with previously published work, *Fgf9*^{null} neonates had shorter humeri (Figure 1C) than WT neonates at P0 (*Fgf9*^{null} $= 3.2 \pm 0.2$ mm, WT $= 2.9 \pm 0.2$ mm).[15] DT migration was measured relative to the length of the humerus (Figure 1D). In *Fgf9*^{null} neonates, the DT was located in a relatively similar position on the humerus compared with WT littermates (Figure 1E,F). Using dynamic bone histomorphometry, *Fgf9*^{null} DTs had an increased and more variable mineral growth rate compared with WT embryos (mineral apposition rate between E16.5 and E18.5: *Fgf9*^{null} $= 133.1 \pm 117.7\%$, WT $= 32.9 \pm 10.7\%$).

2.2 | Global loss of *Fgf9* led to larger attachment-site chondrocyte size but reduced cell proliferation at the attachment

Next, we compared the cellular and matrix morphology of the DT attachment between WT and *Fgf9*^{null} embryos using Hematoxylin and Eosin Y (H&E) staining of transverse histological sections. At E15.5, the size and cell morphology of the DT was similar between WT and *Fgf9*^{null} embryos (Figure 3A,E). At E16.5, the DT of *Fgf9*^{null} embryos appeared larger and less mineralized compared with the DT of WT embryos (Figure 3B,F). At E18.5 and P0, we observed more hypertrophic chondrocytes in the DT of *Fgf9*^{null} mice (Figure 3G,H) compared with WT mice (Figure 3C,D). These hypertrophic chondrocytes stained positive for type X collagen at E16.5 samples (Figure 4). At E16.5, we measured a similar number of hypertrophic chondrocytes at the DT for

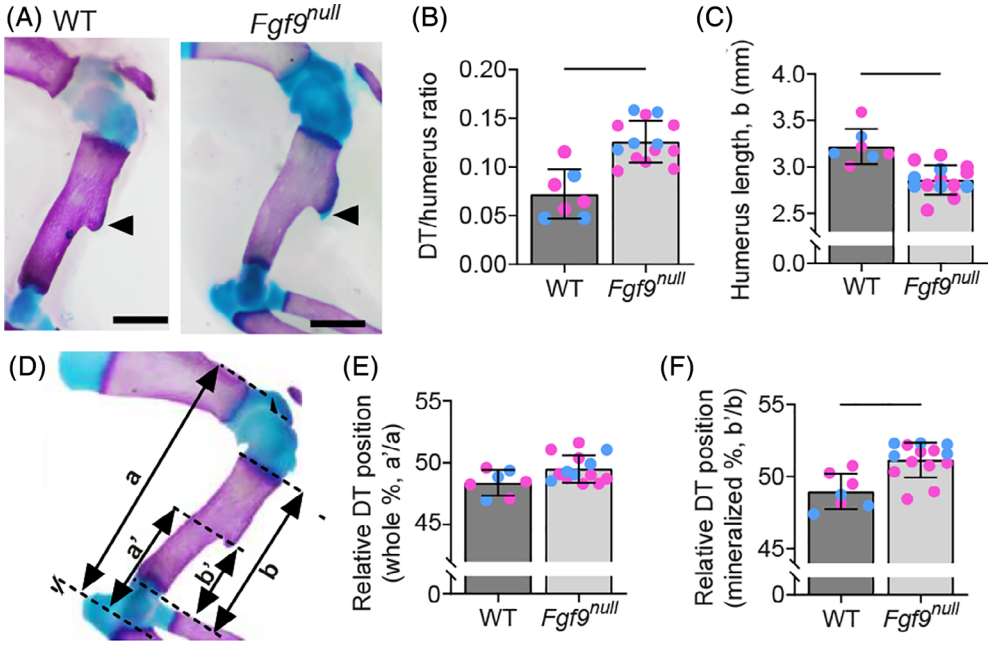

FIGURE 1 The deltoid tuberosities (DTs) of *Fgf9* global knockout (*Fgf9*^{null}) neonates were larger compared with WT neonates. A, Whole mount-stained forearms of a (left) WT mouse and (right) *Fgf9*^{null} neonate at postnatal day 0 (P0) (Scale bar = 1 mm). Black arrows point to the DT, which was noticeably larger on *Fgf9*^{null} neonate humeri. Alcian Blue stain was present on the DT of *Fgf9*^{null} neonates but absent in WT neonates. B, Normalized area of the DT was significantly larger in *Fgf9*^{null} neonates compared with WT neonates at P0. Whether the mice were male (blue) or female (pink) had no effect. C, Contrastingly, the enlarged DT was a part of a shorter mineralized humerus. D, The positioning of the DT on the humerus with respect to the total length, a, a′, and the mineralized length, b, b′. E, Relative to the whole humeri, the DT of *Fgf9*^{null} neonates was in a similar relative location compared with WT neonates. F, Relative to the mineralized region, the DT of *Fgf9*^{null} neonates was more proximally placed than WT neonates. (Data are biological replicates, mean ± SD. Lines in B, C, and F indicate significance ($P < .05$)

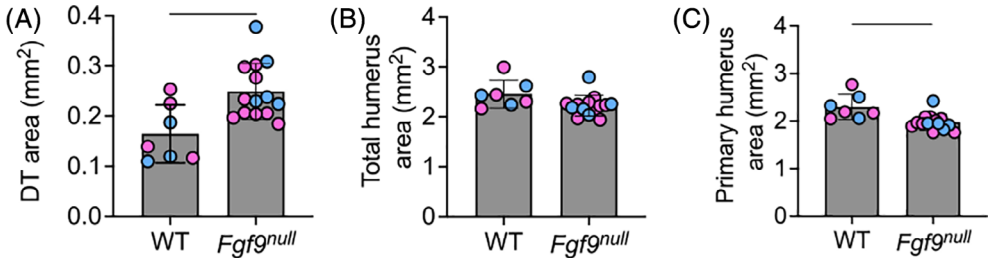

FIGURE 2 *Fgf9*^{null} have a larger DT area with smaller primary humerus area than WT neonates. A, Area of the DT was significantly larger in *Fgf9*^{null} neonates compared with WT neonates at P0. Whether the mice were male (blue) or female (pink) had no effect. B, There was no difference in the combined area of the DT and primary humerus between *Fgf9*^{null} and WT neonates. C, The area of just the primary humerus was significantly smaller in *Fgf9*^{null} neonates compared with WT neonates. Data are biological replicates, mean ± SD; blue = male and magenta = female mice. Lines in A and C indicate significance ($P < .05$)

Fgf9^{null} and WT littermates (Figure 3I). However, the average size of DT-localized hypertrophic chondrocytes in *Fgf9*^{null} embryos at E16.5 was 72% larger compared with WT embryos (Figure 3L). Additionally, cell proliferation at E16.5, visualized using 5-ethynyl-2′-deoxyuridine (EdU), was 51% lower in attachments but not tendons or perichondrium, of *Fgf9*^{null} embryos compared with similar regions of WT embryos (Figure 3N). We did not find measurable differences in cell density (Hoechst-stained; nuclei/100μm^2) between E16.5 WT and *Fgf9*^{null} embryos (Figure 3K).

We visualized mineralization of the attachment using von Kossa staining and found that at E16.5, WT and *Fgf9*^{null} embryos both had a woven mineral pattern within the hypertrophic region. At P0, the remodeled mineral in WT DTs formed a layer of cortical bone (Figure 3Q), whereas in *Fgf9*^{null} neonates, the woven mineral pattern remained (Figure 3U). In addition, fewer osteoclasts were present at both E16.5 and P0 (Figure 3R, V; Figure 5).

2.3 | Global loss of *Fgf9* leads to gene expression differences in muscle, but not bone

Fgf9 is expressed as early as E10.5 in the developing limb and later in the perichondrium and muscle.[15,29-31] At E16.5, *Fgf9*^{null} embryos had increased localized expression of *Gli*, *Sox9*, and *Fgf18* (markers of bone and cartilage development) within and around the DT compared with WT embryos at the same developmental stage (Figure 6B,F,N). At P0, *Fgf9*^{null} neonates had reduced localized *Sox9* and *Sost* expression compared with WT neonates (Figure 6H,L).

For an unbiased comparison of differential gene expression from bone and muscle of WT and *Fgf9*^{null} embryonic limbs, we performed bulk RNAseq from micro-dissected tissue of stylopods at E18.5 (n = 3/genotype). We used a cut-off false discovery rate of 0.05 and discovered 805 differentially expressed (DE) genes between WT and *Fgf9*^{null} muscle with only a single DE gene (*Xist*) in bone. A secondary analysis was performed to exclude DE genes with a fold change greater than two SD between biological replicates. In our secondary analysis, we identified 135 unique genes (Figure 7). The primary and secondary DE gene lists were then analyzed using Database for Annotation, Visualization, and Integrated Discovery (DAVID)[34,35] and the GOTERM cellular components direct, biological processes direct, and molecular functions direct libraries. DE genes in the primary pool of 805 genes were found in a broad set of terms. DE genes in the secondary pool of 135 genes were associated with decreased expression of mitochondria/energy and lipid-associated genes in *Fgf9*^{null} muscle compared with WT muscle (Figure 8). Additionally, of the genes investigated using FISH, we found that *Gli1* was significantly up-regulated in *Fgf9*^{null} muscle compared with WT muscle (fold change = 2.8338; q-value false detection rate = 0.0042). However, *Sox9*, *Sost*, and *Fgf18* were not statistically differentially expressed in muscle. Additionally, none of these genes were significantly differentially expressed between *Fgf9*^{null} and WT bone.

2.4 | Skeletal-muscle specific deletion of *Fgf9* results in enlarged tuberosities and decreased neural-related gene expression

Based on our RNAseq findings, we developed a doxycycline-inducible and skeletal-muscle specific *Fgf9*^{cKO} mouse line, which, unlike *Fgf9*^{null} embryos, were postnatal viable. Muscle-specific targeting was confirmed using the Ai14 tdTomato reporter (*Acta1*-Cre) (Figure 9G,H). At 8 weeks of age, *Fgf9*^{cKO} mice were similar in size and had comparable humerus lengths

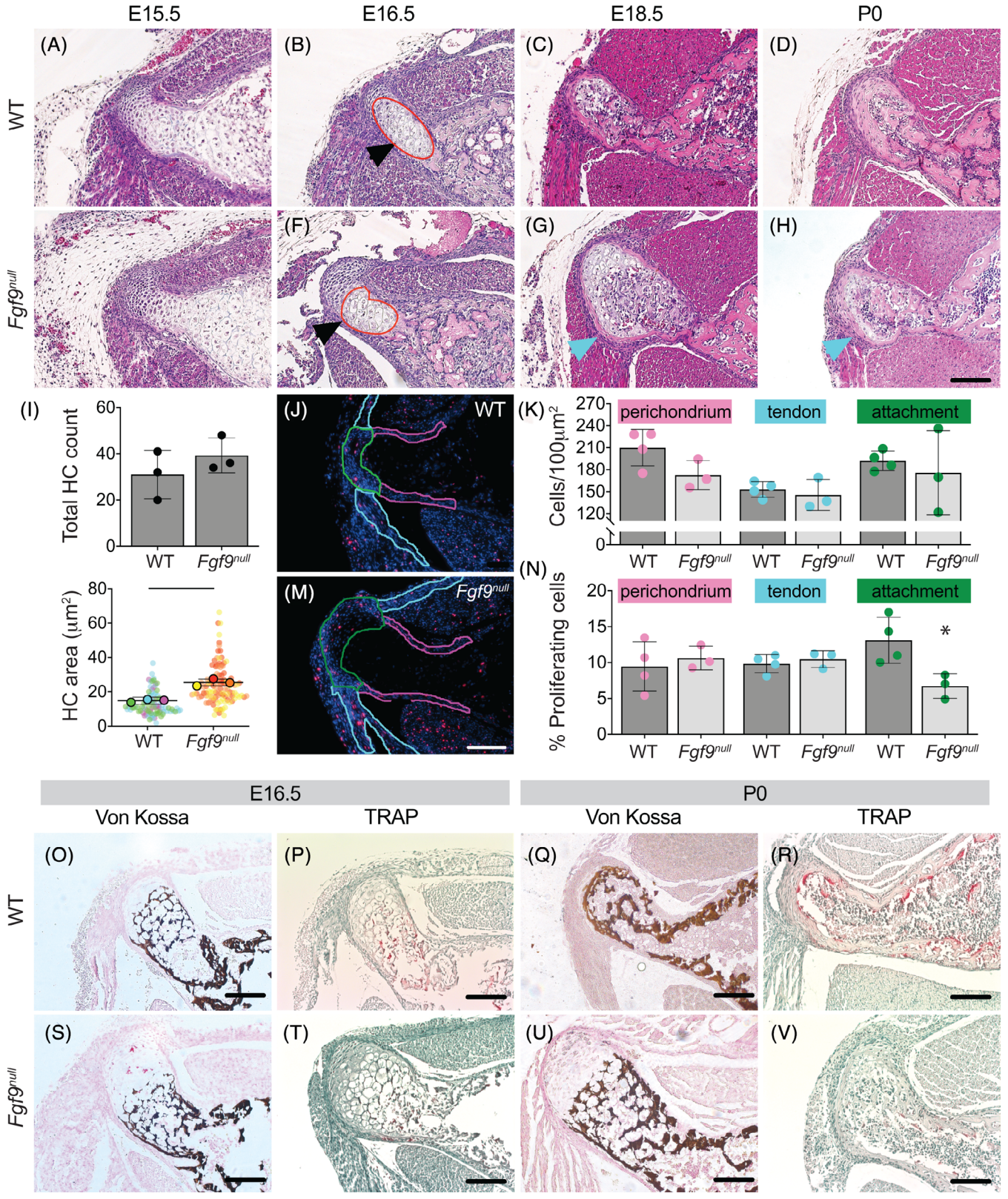

FIGURE 3 Legend on next page.

(Figure 10A) compared with WT littermates. However, *Fgf9*^{cKO} mice had ~35% larger DTs compared with WT littermates by 8-weeks of age (Figure 9C). However, the size of the DT was not measurably different (using microCT) between genotypes at 3-weeks of age, suggesting that the tuberosity is still developing until adulthood (~6-8 weeks

of age). Bone quality of DTs between WT and *Fgf9*^{cKO} mice was similar at 8-weeks of age (Figure 10B). In addition, another bony superstructure on the humerus, the lateral supracondylar ridge (LSR) near the elbow where extensor muscles originate, was ~30% larger in *Fgf9*^{cKO} mice than WT mice (Figure 9D). Gene expression of *Agrn* (Figure 9I) and *Ikbkb* (Figure 9J, not statistically significant) in deltoid muscle from *Fgf9*^{cKO}mice was increased compared with WT mice at 8 weeks but not 3 weeks of age. Acetylcholine receptor (AChR) density (Figure 9N) was 30% significantly higher in the deltoid muscles of *Fgf9*^{cKO} mice when compared with that of WT mice at 3 weeks of age (Figure 9K,L). However, AChR density normalized between genotypes by 8 weeks. There was not a significant difference in total AChR count in the deltoid for either time point (Figure 9M).

3 | DISCUSSION

3.1 | Intrinsic vs. extrinsic roles of FGF9 in DT development

In this study, we showed that *Fgf9* may act as a negative regulator in growth of attachment superstructures such as the DT. Global deletion of *Fgf9* led to enlarged superstructure size, and these superstructures had altered endochondral ossification of the arrested growth plate. This phenotype of enlarged DTs was modestly matched in conditional knockout of *Fgf9* in skeletal muscle, suggesting a potential nonautonomous role of FGF9 during DT growth. The decreased proliferation we have shown in DTs of *Fgf9*^{null} embryos, as well as enlarged hypertrophic chondrocytes, is similar to findings from

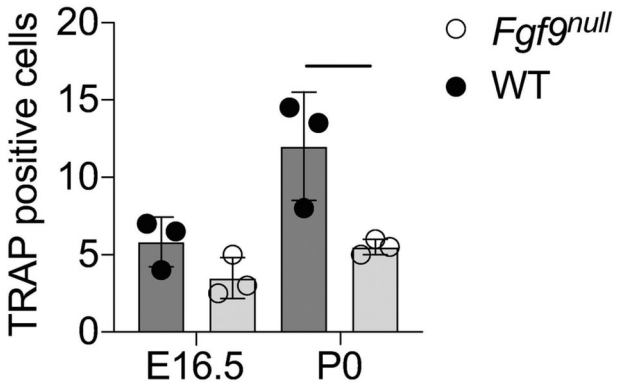

FIGURE 5 Fewer osteoclasts present in *Fgf9*^{null} DTs. *Fgf9*^{null} mice have fewer osteoclasts at E16.5 and significantly fewer osteoclasts at p0. Data are biological replicates (1-2 technical replicates averaged per sample) mean ± SD. Line indicate significance ($P < .05$)

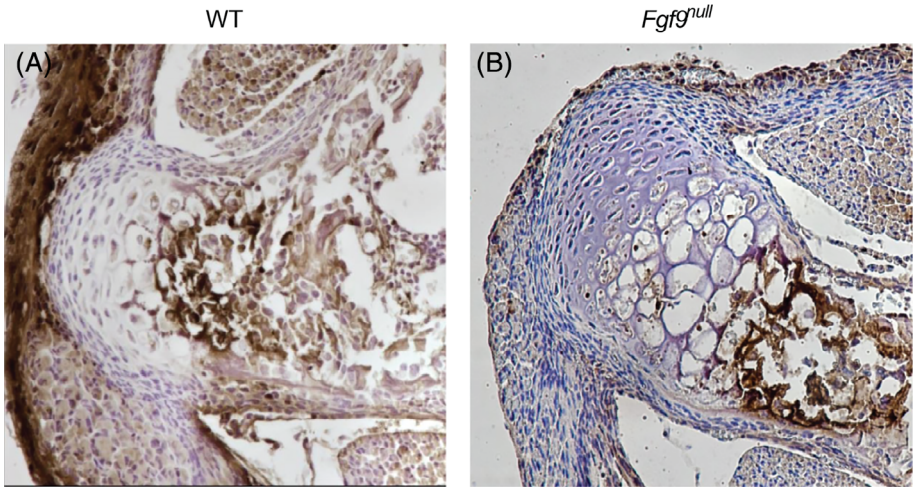

FIGURE 4 Type X collagen immunostaining of the DT in WT and *Fgf9*^{null} embryos at E16.5. The tendon attachment has less ColX staining but more ColX+ hypertrophic cells in *Fgf9*^{null} attachments compared with WT attachments

FIGURE 3 The DTs of *Fgf9*^{null} embryos undergo differences in cellular and morphological development when compared with WT embryos. The DT of *Fgf9*^{null} embryos was larger than the DT of WT embryos as early as E16.5 (black arrows; scale bar = 100 μm). During later stages of development (E18.5, C, G, and P0, D, H), hypertrophic chondrocytes (blue arrows) remained in the DT of *Fgf9*^{null} embryonic limb and were absent in WT embryonic limb. H&E-stained transverse sections of the DT in, B, WT embryos and F, *Fgf9*^{null} embryos at E16.5. Red lines represent the region of hypertrophic chondrocytes. *Fgf9*^{null} embryos had a, I similar number of hypertrophic chondrocytes and, L, larger average area of hypertrophic chondrocytes compared with WT embryos. J,M, Proliferating cells were labeled at E16.5 using EdU, in red. Outlined regions of interest include the perichondrium (pink), tendon (teal), and attachment (green). *Fgf9*^{null} embryos had, K, similar cell density and, N, reduced proliferation rates at the DT attachment compared with WT embryos at E16.5. U, At P0 *Fgf9*^{null} neonates had abnormal mineral patterning (von Kossa) and, V, fewer osteoclasts (TRAP) than, Q,R, WT neonates (scale = 100 μm). Data are biological replicates (faded circles are technical replicates), mean ± SD. Lines in L and * in N indicates significant difference between groups ($P < 0.05$)

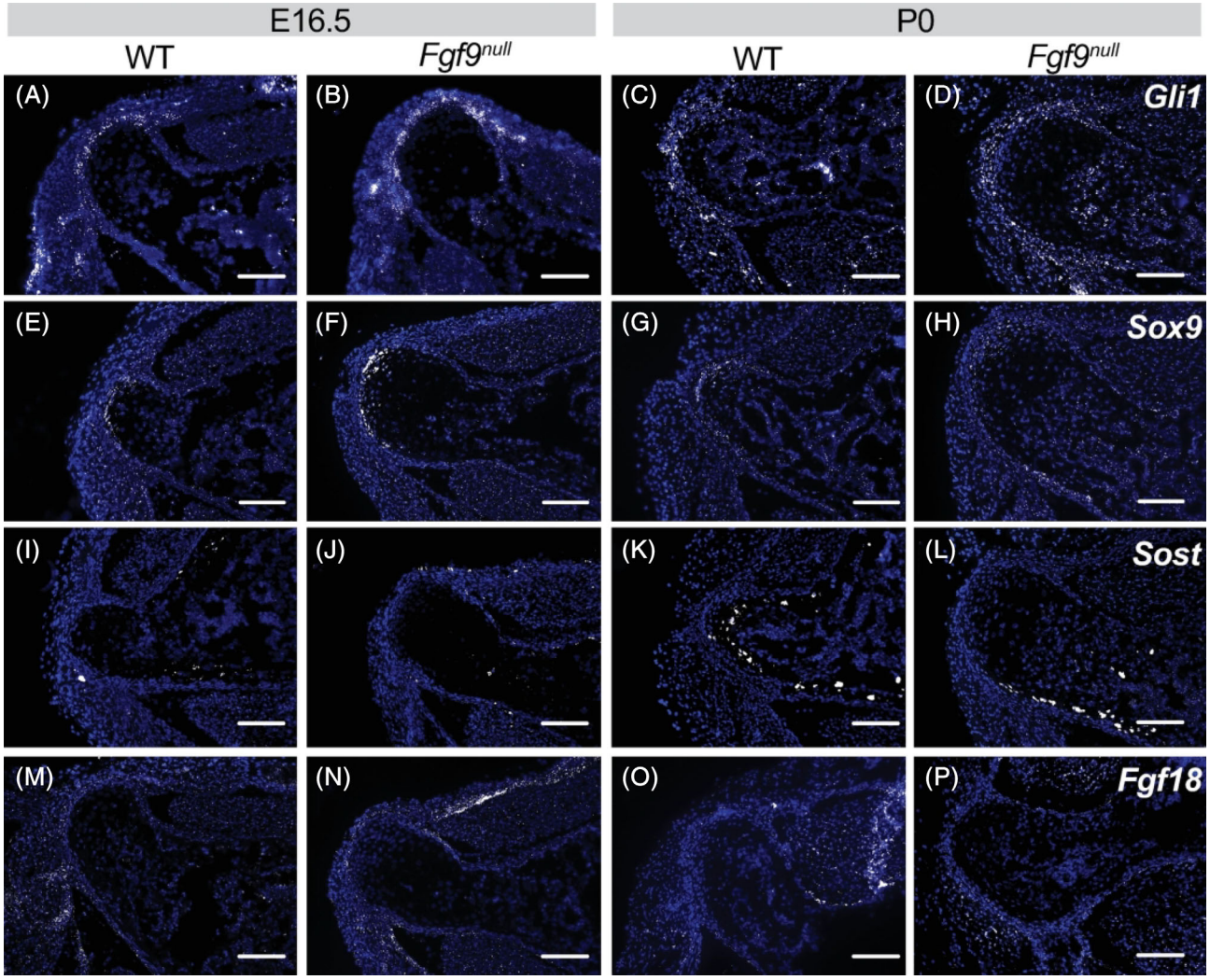

FIGURE 6 Fluorescent in situ hybridization (FISH) of, A-D, *Gli1*, E-H, *Sox9*, I-L, *Sost*, and, M-P, *Fgf18* at E16.5 and P0 of $Fgf9^{null}$ and WT mice. At E16.5, $Fgf9^{null}$ embryos had increased, B, *Gli*, F, *Sox9*, and, N, *Fgf18* expression compared with (A,E,I,M) WT embryos. At P0, $Fgf9^{null}$ neonates had less, H, *Sox9* and, L, *Sost*, and similar, D, Gli1 and, P, *Fgf18* expression compared with, C,G,L,P, WT neonates (scale bar = 100 μm; n = 3 per genotype for each time point)

previous work studying long bone development of $Fgf9^{null}$ embryos.[15,16] The prevalence of hypertrophic chondrocytes at the tendon attachment in $Fgf9^{null}$ embryos may be suggestive of a prolonged progenitor cell maintenance along with these superstructures.[7] *Sox9* and hedgehog signaling (e.g., *Gli1*) are sequentially required for cellular expansion of growth plates during endochondral bone formation[36-41]; however, migratory attachments (like the DT) form via replacement of *Sox9* expressing cells by *Gli1* expressing cells.[12] At E16.5, as DT enlargement begins in $Fgf9^{null}$ embryos, we observed increased *Gli1* and *Sox9* expression around the attachment. Indian hedgehog signaling also represses transcription of hypertrophy-related genes,[42] and inhibits parathyroid hormone-like hormone (*Pthlh*) activity to maintain chondrocytes in a proliferative stage.[43] Though we saw similar levels of *Pthlh* expression in both WT and $Fgf9^{null}$ attachments, we did measure a decrease in cell proliferation in $Fgf9^{null}$ attachments, suggesting an accelerated chondrocyte maturation. This was supported by increased *Gli1* expression in $Fgf9^{null}$ attachments compared with WT attachments. This decrease in proliferation was in parallel with increased hypertrophy of chondrocytes adjacent to the attachment cells within the $Fgf9^{null}$ DT, which may have led to a rapid expansion of matrix in the DT. Even though the DT was enlarged in $Fgf9^{null}$ mutants, we found fewer *Sost* + cell clusters in their DTs compared with WT mice. Mature osteocytes express *Sost*,[44] and fewer *Sost* + cells may indicate an impaired ability of $Fgf9^{null}$ osteoblasts to embed and mature into osteocytes. Overexpression of FGF9 in the perichondrium has been previously shown to suppress

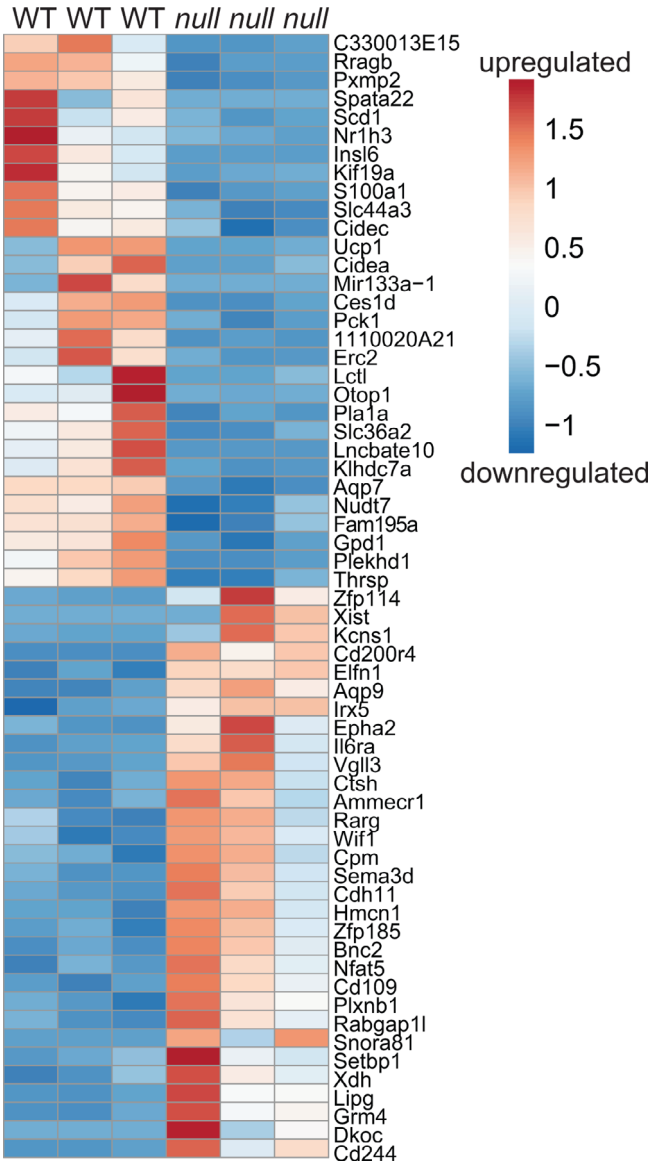

FIGURE 7 Heat map of top 30 up-regulated and downregulated genes from RNASeq secondary analysis of embryonic WT and *Fgf9*^{null} muscle. Hundred and thirty-five differentially expressed (DE) with a false discovery rate value <.05 and genes omitted with fold change outside 2 SD of genotype average log2 fold change (FC). Color indicates z-score value as calculated and presented using Morpheus software. Scale bar = log2 FC

chondrocyte proliferation and limit bone growth in the limb[26]; in our study, we found that loss of *Fgf9* globally leads to an accelerated enlargement of chondrocytes in the tuberosity. This accelerated enlargement may limit the ability of these cells to deposit matrix and mineral and therefore limit osteocyte differentiation. We also found fewer osteoclasts in the *Fgf9*^{null} DT which mirrors previous reports using the same mutation to study the length and vascularity of developing limb.[15] Because the DT is enlarged and resides on the surface of a shortened bone, this phenotype may elucidate a divergent role of FGF9 in patterning of an arrested (e.g., attachment) growth plate compared with a regular (e.g., long bone) growth plate. This includes unexplored roles of FGF9 in vascularity of the tendon attachment and formation of bone ridges that overlap with or deviate from its role in growth plate development that are beyond the scope of the current study.

FGF ligands have varying affinities for receptors, and receptor expression changes throughout cell development.[20] The primary receptors of FGF9 during musculoskeletal development are *Fgfr1*, *Fgfr2*, and *Fgfr3*. *Fgfr1* is highly expressed in hypertrophic chondrocytes,[45] *Fgfr1* and *Fgfr2* are co-expressed in osteogenic cells,[21,45] and *Fgfr3* is predominately expressed in proliferating chondrocytes.[46] Given the striking role of *Fgf9* deletion on tuberosity development shown in our study, FGF signaling may play a unique and cell-specific role during the establishment and growth of the *Sox9/Scx* progenitor pool found within developing superstructures.[7] Previous work in craniofacial development has shown that *Fgfr2* expression is necessary for maintaining *Sox9/Scx* progenitor pool cell fate[47]; however, spatial differences and regulatory roles of *Fgf* signaling between craniofacial and limb development are important to consider. For example, within the developing humerus, progenitor cell pools are temporally and transcriptionally different depending on location (e.g., proximal DT vs. distal olecranon superstructures).[48] Additionally, *Fgf9* predominantly effects proximal (stylopod) skeletal elements rather than distal (zeugopod, autopod) elements.[15] Thus, the timing, spatial contribution, and expression patterns of *Fgf9* on musculoskeletal development may be isolated to certain cells in proximal elements.[15,20]

The enlargement of the DT in *Fgf9*^{null} embryos may also suggest differential rapid growth, as seen in the growth plate of some long bones in jerboa and bat.[49,50] For example, Cooper et al showed that average chondrocyte volume was larger in the growth plate of the jerboa metatarsal compared with the mouse metatarsal, and the jerboa foot elongates 2.5 times more proportionally compared with the mouse foot.[49,51] Additionally, increased proliferation and greater elongation of forelimb digits in bats compared with mice are likely driven by increased size of hypertrophic chondrocytes, which is predominantly mediated by BMP signaling.[50] It is possible that the enlarged chondrocyte phenotype we observe histologically in the DT is an extended and accelerated growth of cell volume.[49] Notably, in our study, we did not see an increase in cell proliferation, which is attributed in part to rapid elongation of bat metatarsals.[50,52] This divergent developmental pattern could differentiate the growth of

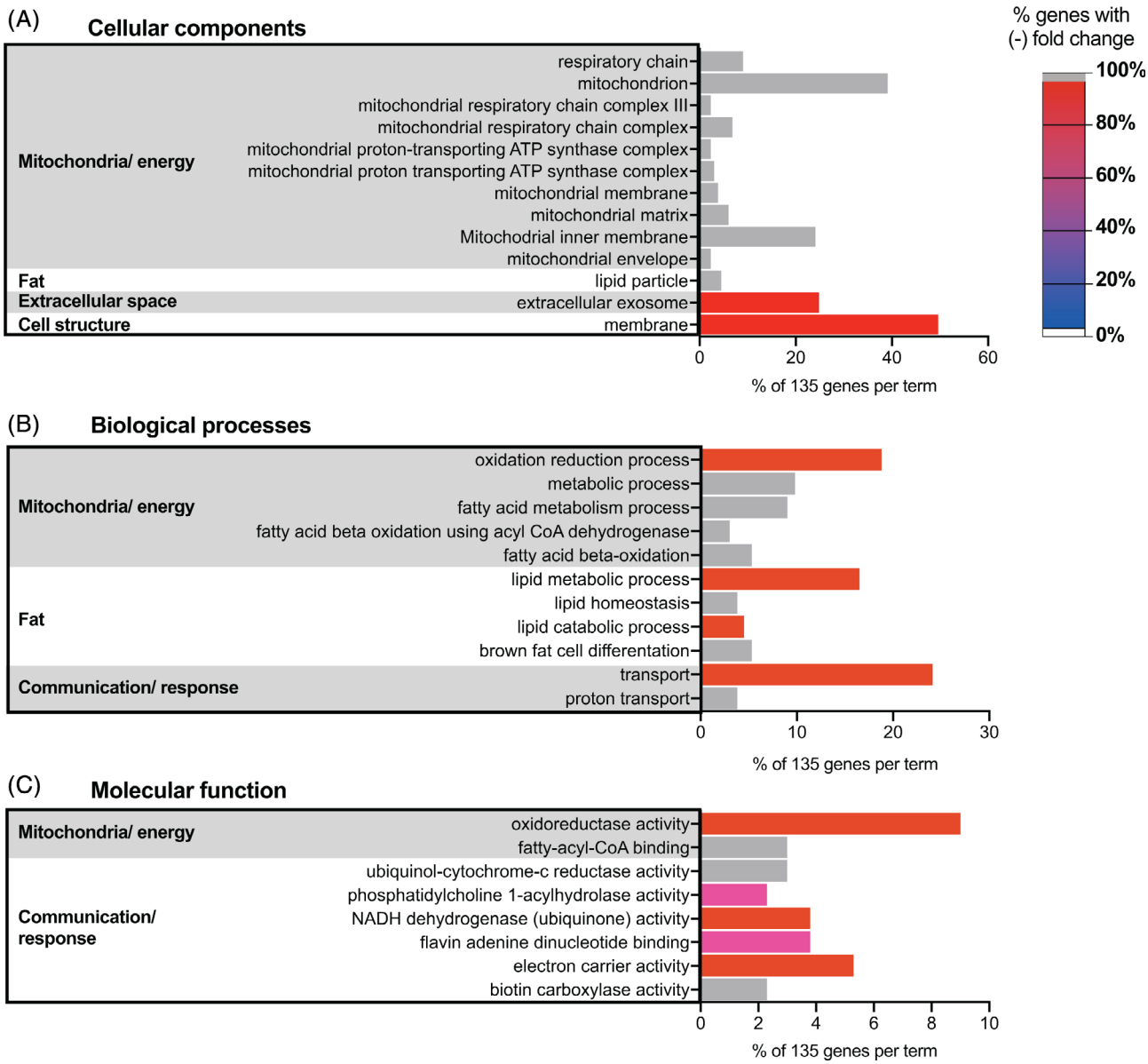

FIGURE 8 *Fgf9*^{null} muscle had predominantly downregulated mitochondrial and energy-related gene expression compared with WT muscle. Hundred and thirty-five differentially expressed (DE) genes from secondary analyses were categorized using DAVID against a *Mus musculus* background. Terms with a Benjamini value <.05 were selected from the, A, GOTERM cellular components DIRECT, B, GOTERM biological processes DIRECT, C, and GOTERM molecular function DIRECT. Similar terms were then clustered into categories (bar chart = % gene in term out of 135; color = % genes in term with negative fold change). Terms with 100% negative FC (WT vs. *Fgf9*^{null}) were assigned gray bars

arrested growth plates in superstructures like the DT from long bone growth plates.

3.2 | Role of FGF9 in myogenesis

Fgf9 is expressed in muscle during embryonic stages, which we and others have observed using ISH.[15,29-31] Previous work has established a connection between *Fgf9* and muscle, as treatment of muscle and muscle progenitor cells with FGF9 slows maturation, enhances proliferation, and decreases expression of various myogenic genes.[53] This study found supporting evidence that *Fgf9* expression in muscle may be a limiting factor in tuberosity growth. However, it remains unknown how other FGFs and their receptors, FGFRs, regulate superstructure and attachment formation. In this study, we identified potential mediators of skeletal muscle metabolism in *Fgf9*^{null} muscle, including downregulated mitochondrial-related genes associated with oxidative

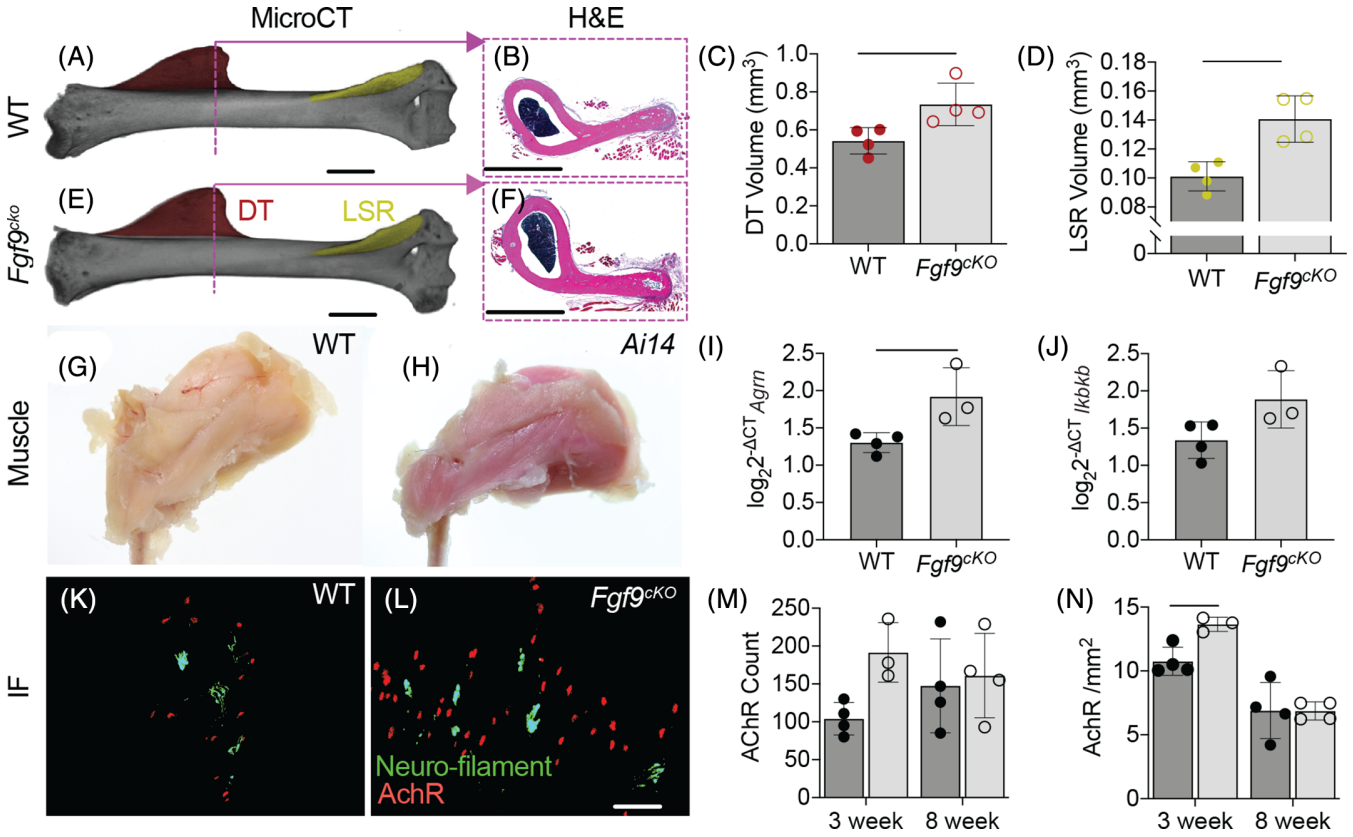

FIGURE 9 Muscle-specific knockout of *Fgf9* in mice ($Fgf9^{cKO}$) resulted in larger superstructures and increased number of acetylcholine receptor (AChR) clusters in the deltoid muscle. MicroCT scans of 8 week, A, WT and, E, $Fgf9^{cKO}$ mice show a significantly larger DT (DT; red) and lateral supracondylar ridge (LSR; yellow) in $Fgf9^{cKO}$ mice. Histology of the DT support this phenotype, B, F. Skeletal muscle specificity of *Acta1*-Cre was confirmed using Ai14 reporters, H,G. Gene expression of, I, *Agrn* ($P = .0287$) and, J, *Ikbkb* ($P = .0675$) were increased in $Fgf9^{cKO}$ deltoid muscle compared with WT muscle at 8 weeks of age (ΔCT calculated using average reference gene CT of *ipo8* and *Rn18s*). Immunofluorescence (IF) was used to visualize nerves (neurofilament, green) and AChR clusters at neuromuscular junctions (α-bungarotoxin, red) in, K, WT and, L, $Fgf9^{cKO}$ mice. At 3 weeks postnatally, $Fgf9^{cKO}$ mice had significantly higher, N, AchR density than WT littermates and, M, more AChR. Data shown are biological replicates, mean ± SD. Lines in C, D, I, and N indicate significance ($P < .05$)

respiration and proton transport (i.e., *Slc36a2* and *Ucp1*, among others). In cultured myoblasts, FGF9 can inhibit myogenic differentiation potentially via increased production of *Myostatin*,[53] a well-established mediator of fast glycolytic muscle fibers.[54,55] While the role of FGF9 in myoblast fusion has been investigated in vitro, its effect on muscle fiber type and fiber metabolism (i.e., oxidative vs. glycolytic) has not yet been explored. Our findings from bulk RNA-seq of $Fgf9^{null}$ muscle point to potential mechanisms in muscle metabolism that may contribute to the enlarged phenotype that is mimetic of that found in *Myostatin* deficient mice and other animals.[14,56] Conversely, following muscle paralysis in the developing duck jaw, the secondary cartilage at tendon entheses is lost.[57] Additionally, this study found that expression of *Fgfr2* in the enthesis of the duck jaw was regulated by activation of stretch-sensitive ion channels.[57] Further investigations are needed to investigate the potential role of *Fgf9* in mitochondrial function, ion transport, and lipid metabolism. Recent work by Huang et al also identified FGF9 as a potent regulator of calcium signaling and homeostasis in myoblast culture in vitro, and calcium release from the sarcoplasmic reticulum in muscle plays a critical role during embryonic skeletal myogenesis via ryanodine receptor 1 (RYR1).[53] Although *Ryr1* was not significantly different in between $Fgf9^{null}$ and WT muscle in the present study, we did find that calmodulin-associated genes (e.g., *Calm4*, *Calml3*, *Camsap3*, and *Calm5*) were all significantly up-regulated in $Fgf9^{null}$ muscle compared with WT muscle. Calmodulin interacts with RYR1 and its activation is required for intracellular binding of calcium.[58(p1)] Calmodulin is a crucial component of the calcium signal transduction pathway and also plays an important role in lipid and glucose metabolism.[59] Taken together, our findings along with recent work by Huang et al support more mechanistic studies to investigate the metabolic effects of loss and gain of function of *Fgf9* on skeletal muscle as well as the muscle secretome.

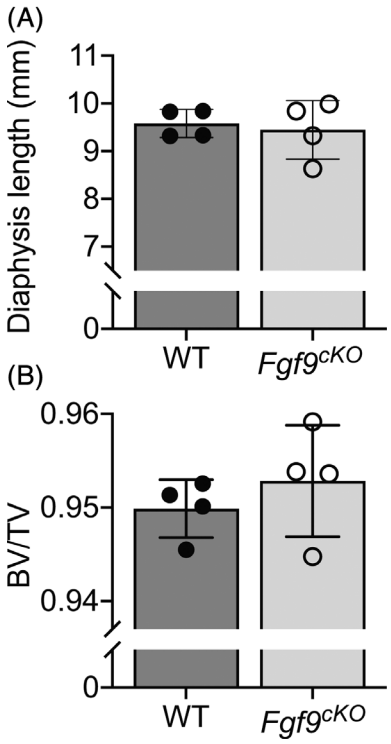

FIGURE 10 No difference in humerus length and DT bone volume/total volume (BV/TV) between $Fgf9^{cKO}$ and WT mice. MicroCT scans of 8-week samples showed that, A, $Fgf9^{cKO}$ mice had a humerus of similar length when compared with WT littermates. B, Though the DT was larger, BV/TV in $Fgf9^{cKO}$ and WT littermates. Data are biological replicates, mean ± SD

In conclusion, this work established a new role of skeletal muscle derived *Fgf9* during skeletal development and tuberosity growth. Additionally, our unbiased transcriptomic approaches and rigorous analyses identified new potential mechanisms associated with muscle development, mitochondrial bioenergetics, and muscle metabolism that warrant further investigation into the role of FGF9 in muscle-bone crosstalk.

4 | EXPERIMENTAL PROCEDURES

4.1 | Mice

Prrx1-Cre, Ai14(RCL-tdT)-D (Ai14), and Acta1-rtTA-tetO-Cre (*Acta1*-Cre) transgenic mice were obtained from Jackson Laboratory (The Jackson Laboratory, Bar Harbor, Maine). *Fgf9*-floxed mice were generated as previously described.[29,60] Mice carrying the *Fgf9* excised allele were maintained on a C57BL6J background. All experiments were performed with approval from the University of Delaware and University of Michigan Institutional Animal Care and Use Committees.

4.2 | Breeding and genotyping

For global mutants, $Fgf9^{ex/WT}$; *Prrx1*-Cre female mice were bred with $Fgf9^{flx/flx}$ male (mixed background) mice to generate pups with homozygous excised *Fgf9* alleles ($Fgf9^{null}$) and $Fgf9^{WT/Ex}$ (WT) littermates. The exploitation of the *Prrx1*-Cre female donors resulted in global excision of floxed alleles in utero, thereby generating global knockouts.[60] Embryos and neonates were used for all experiments. For timed matings, we considered noon on the day following mating as 0.5 days post coitum (0.5 dpc). For muscle-specific knockouts, $Fgf9^{flx/WT}$; *Acta*1-Cre mice were crossed with $Fgf9^{flx/flx}$ mice and dams were given doxycycline chow ad libitum throughout gestation and weaning. To confirm that muscle was being targeted, *Acta1*-Cre mice were crossed with Ai14 reporter mice and dams were also given doxycycline chow ad libitum throughout gestation and weaning. Muscle targeting was confirmed via red fluorescent protein expression in Ai14; *Acta1*-Cre mouse muscle (Figure 6H). Genotypes were determined by PCR using commercial vendors (Transnetyx, Cordova, Tennessee). The efficiency of Cre-recombination and confirmation of $Fgf9^{null}$ gene knockout was determined using quantitative reverse transcription-polymerase chain reaction (qRT-PCR) (WT n = 3; $Fgf9^{null}$ n = 3). RNA was isolated from whole limbs using phenol/chloroform and on-column commercially available kits (Invitrogen, ThermoFisher). RNA was converted to cDNA at 5 ng/μl concentrations for all samples using Superscript (VILO, ThermoFisher) and cDNA samples were amplified as technical replicates (in triplicate) using SYBR green (PerfeCTa, QuantBio) and primers (IDT). ΔCT values were calculated using *Rn18s* as the reference gene. Relative expression was then calculated using $2^{-\Delta CT}$. Gene expression of Fgf9 was not detected and Scx expression was reduced in $Fgf9^{null}$ limbs (Figure 11).

4.3 | Measurement of DT size

For global mutants, whole-mount staining was used following a standard protocol.[61] Arms of P0 neonates (WT n = 7; $Fgf9^{null}$ n = 14) were removed from whole-mount skeletons and placed in a Petri dish filled with glycerol with the anterior side facing up. In-plane with the arm, we used a ruler at the bottom of the petri dish for scaling. Samples were imaged using a Stemi dissection microscope (Carl Zeiss, Gottingen, Germany) and imaged using (EOS REBEL T5, Canon, Melville, New York). The size of the DT and humerus were measured using ImageJ.[62] When we observed no significant difference in mineralized humerus area and DT area

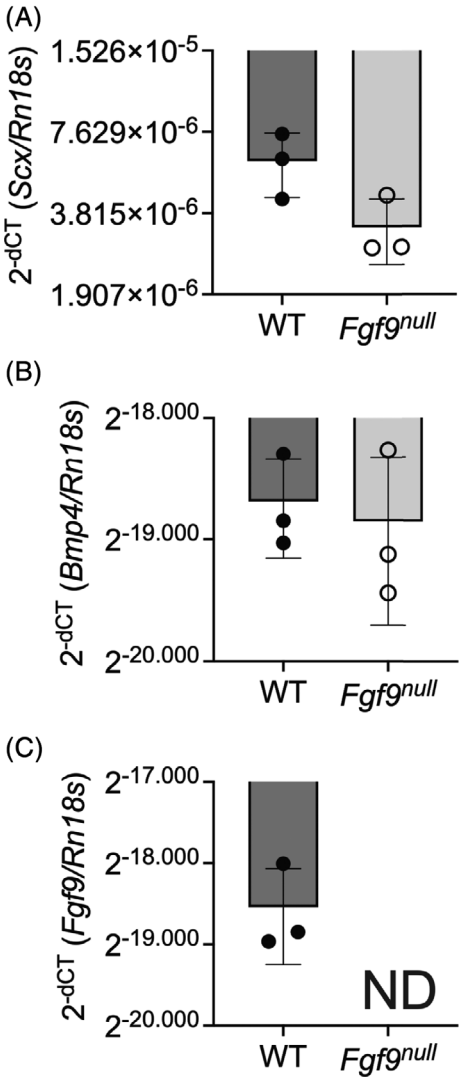

FIGURE 11 Gene expression of, A, *Scx*, B, *Bmp4*, and, C, *Fgf9* from WT and *Fgf9*^{null} embryonic limbs at E18.5. Relative expression are biological replicates ($2^{-\Delta CT}$), mean ± SD. ND = not detected or CT value greater than or equal to 35

combined (Figure 2B), we based DT size on the ratio of DT area to mineralized humerus area. Red mineral staining determined the mineralized zone, and DT measurement included any cartilage observed at the crest of the DT. We determined the relative placement of the DT based on a ratio of length distal to DT over the length of the humerus. Both mineralized humerus and full humerus were measured. The distal length was based on the distance between the most distal part of the DT and the most distal part of the mineralized/full humerus. Humerus length was based on the distance between the most proximal part of the mineralized/full humerus and the most distal part of the mineralized/full humerus. Once we determined no difference between left and right arms, values were averaged together.

4.4 | Histology and in situ hybridization

Embryonic and neonatal mice were eviscerated and fixed in 4% paraformaldehyde (PFA) for 24 hours. Forelimbs for histology of a subset of embryonic age 18.5 (E18.5) embryos and P0 neonates were decalcified using formic acid (Formical 2000, Statlab, McKinney, Texas) for 24 hours. Histomorphometry was carried out on 7 μm paraffin sections of samples from E15.5 to P0 (n = at least 3 per genotype/time point). Samples were stained using hematoxylin and eosin (H&E), coverslipped with acrymount (Statlab, McKinney, Texas), and imaged with an Upright microscope (Carl Zeiss, Gottingen, Germany). The area and number of hypertrophic chondrocytes were measured in the DT of E16.5 embryos using the freehand and multipoint tools in ImageJ.[62] Non-decalcified E16.5 and P0 samples had mineralized bone visualized by von Kossa staining (n = 3 per age and genotype) with Nuclear Fast Red counterstaining as part of an established protocol (Abcam, Cambridge, UK). For osteoclast staining, P0 neonates were decalcified using 14% ethylene-diamine-tetraacetic acid (EDTA), paraffin sectioned, and stained for TRAP (n = 3 per age and genotype). We performed in situ hybridization using the RNAscope Multiplex Fluorescent Reagent Kit v2 (Advanced Cell Diagnostics, Hayward, California). Non decalcified E16.5 and P0 samples (n = 3 per age and genotype) were treated with *Fgf9*, *Fgf18*, *Gli1*, *Pthlh*, *Scx*, *Sost*, *Sox9*, *and Wnt7b* probes (Advanced Cell Diagnostics, Hayward, California) for 2 hours at 40C. A positive control slide used a mixture of probes targeting housekeeping genes *Polr2A*, *Ppib*, and *Ubc*. A negative control slide used dapB (a bacteria gene). Nuclei were counterstained with DAPI and mounted with Citifluor Antifade mounting medium (Electron Microscopy Science, Hatfield, Pennsylvania). Slides were imaged using Zeiss Axio-observer Z1 microscope (Axio. Observer Z1, Carl Zeiss, Gottingen, Germany).

4.5 | Immunohistochemistry

Embryonic and neonatal mice were eviscerated and fixed in 4% PFA for 24 hours (n = 3 age and genotype). Forelimbs for histology of P0 neonates were decalcified using 14% EDTA for 24 hours. Histomorphometry was carried out on 7 μm paraffin sections of samples from E15.5 and P0 (n = at least 3 per genotype/time point). Slides were deparaffinized and hydrated to 70% ETOH, followed by heat mediated antigen retrieval (Sodium Citrate Buffer, pH 6.0) at 65°C for 2 hours. Slides were kept in the solution until equilibrated to room temperature, quenched in 0.3% hydrogen peroxide (Santa Cruz, Dallas, Texas) for

30 minutes and blocked with 5% goat serum in 1% phosphate buffer saline in room temperature for 1 hour. For primary antibody, rabbit monoclonal anti-collagen X antibody (ab260040; 1:1000 dilution) (ABCAM, Cambridge, Massachusetts) was used for overnight incubation at 4°C. Following incubation, HRP/DAB system (Millipore Sigma) was used for detection. Samples were then counterstained with hematoxylin and mounted with a xylene-based mounting medium (Acrymount, Stat Lab, McKinney, Texas) and imaged using a Lionheart FX (BioTek, Winooski, Vermont). 2 P0 (n = 1 per genotype) samples were omitted from analysis due to surplus nonspecific staining.

4.6 | EdU proliferation

A dam at E16.5 in gestation was given an intraperitoneal (IP) injection with EdU (5-ethynyl- 2′-deoxyuridine) from the Click-iT EdU Alexa FluorTM 647 Imaging Kit (Invitrogen, Carlsbad, California) at a dosage of 0.25 mg/10 g body weight. The dam was euthanized 2 hours later using CO_2 asphyxiation. Embryos were eviscerated and fixed in 4% PFA for 24 hours. Forelimbs were processed for paraffin histology, and humeri were cut in the transverse plane at 7 μm. Proliferating cells were stained with Alexa Fluor 647 and Hoechst 33342 as a counterstain. Slices were mounted with Citifluor Antifade mounting media. Two histological sections per sample treated with EdU (WT n = 4; *Fgf9*^{null} n = 3) were imaged using a Zeiss Axio-Observer Z1 microscope (Zeiss, Gottingen, Germany). Differential interference contrast (DIC) images and fluorescence images were collected from the same observed tissue to visualize tissue morphology. DIC allowed us to observe the highly organized structure of the tendon and perichondrium. Regions were separated into perichondrium, tendon, and attachment. Tissue area, nuclei number, and the number of EdU positive proliferating cells were measured and counted within ImageJ using the freehand and multipoint tools. Two slides per sample were averaged together. For the tendon and perichondrium, tissues on the medial and lateral side of the DT were measured separately. Once no phenotypic difference based on the side of tissue was observed, medial and lateral values were summed together.

4.7 | Evaluation of bone deposition and resorption

For dynamic bone histomorphometry, Calcein (Sigma, C0875; 15 mg/kg body weight; 12 PM) was injected into pregnant females intraperitoneally (IP) at E16.5 and Alizarin Complexone (Sigma, a3882; 45 mg/kg IP; 2 days later at 6 PM) at E18.5 with a set time in between of 42 hours. Neonates were collected at birth, eviscerated, and fixed for 24 hours in 4% PFA. After paraffin embedding, samples were sectioned at 7um. Slides were deparaffinized, dehydrated, and mounted with Acrymount. Slides were imaged using Zeiss Axio-observer Z1 microscope (Zeiss, Gottingen, Germany). Calcein Green and Alizarin Red were imaged using fluorescence microscopy and quantified using ImageJ by using the freehand tool to measure the area of green and red stained mineral. The mineralization area (MA) of the DT was measured, and the mineral growth rate was calculated using:

$$\text{Growth rate} = ((\text{MA}_{\text{E18.5}}) - (\text{MA}_{\text{E16.5}}))/(\text{MA}_{\text{E16.5}})\,\text{x}\,100 \quad (1)$$

4.8 | Bulk RNA-sequencing

E18.5 embryos were collected, toed, and eviscerated under sterile conditions. RNA was extracted from each sample (n = 3 WT and n = 3 *Fgf9*^{null}) using Trizol/chloroform and spin-column assembly with on-column DNase treatment (RNeasy mini kits; Qiagen Germantown, MD). We assessed the quality of RNA using fragment analysis to obtain RNA integrity number (RIN) before proceeding with Library preparation (NEBNext Ultra RNA Library Prep Kit, Illumina, San Diego, California). Each sample was sequenced in Illumina HiSeq 2000 (Single read, 50 base pair). Sequence reads from each sample were quality assessed (FastQC) & all the reads were quality trimmed and filtered (threshold length of the sequence was 30 and Phred score of each base was 28). Reads were mapped to the *Mus musculus* reference genome (mm10) using TopHat2 with default settings (ver 2.1.0)[63] and mapping quality control metrics were obtained for RSeQC (ver 2.6.1).[64] Per gene counts were determined using HTseq (ver 0.6.1p1)[65] and used for pairwise determination of differential expression analyses using EdgeR (ver 3.28.1)[66] with a significance cutoff of FDR-corrected $P < .05$. To control for consistency within biological replicates, a secondary analysis was performed to exclude DE within a group if the mean count per million for a gene feature in each sample was >log2FC different than its biological replicates (yielding 135 genes). These 135 genes were then uploaded to Morpheus, which assigned a z score to determine the top 30 up-regulated and downregulated genes and generate a heatmap (Morpheus, https://software.broadinstitute.org/morpheus). Both sample pools (primary analysis of 805 and secondary analysis of 135) were then uploaded to

DAVID Bioinformatics Resources 6.8 [34,35] and run against a mm10 background. GOTERM cellular components direct, GOTERM biological processes direct, and GOTERM molecular functions direct libraries were examined, and terms were ranked based on Benjamini number (DAVID adjusted *P* value).[67] Terms with a Benjamini number < .05 were percentiled and categorized based on similarity.

4.9 | Skeletal muscle immunofluorescence

Muscle-specific *Fgf9* knockouts and WT littermates were euthanized at 3 weeks of age (n = 4 WT, n = 3 $Fgf9^{cKO}$) and 8 weeks of age (n = 4 WT, n = 4 $Fgf9^{cKO}$) for histology, structural analysis, and RNA isolation. Immediately following euthanasia, the right deltoid muscles of each mouse were dissected in an RNase-free environment, flash-frozen in liquid nitrogen, and stored at −80°C until RNA isolation. The left deltoid muscles were then dissected, fixed in 4% PFA for 20 minutes, cryo-protected, and then embedded in optimal cutting temperature (OCT) media for cryosectioning (longitudinal plane). The left humerus from each mouse was also dissected, fixed in 4% PFA, and stored in 70% ethanol.

The immunofluorescence staining protocol used in this study was based on previously established protocol.[68] For 3- and 8-week-old deltoids, 35 μm thick sections were used immunohistochemistry (IHC) of acetylcholine receptors (α-Bungarotoxin extracted from Bungarus muticinctus, conjugated to Alexa Fluor 647, Thermofisher #B35450) and nerve fibers (chicken anti-neurofilament-H antibody, Thermofisher #PA1-10002; Alexa Fluor 488 donkey anti-chicken, Jackson Immunofluorescence #703-545-155). Samples were then imaged using a Zeiss Axio-observer Z1 microscope (Zeiss, Gottingen, Germany) at ×20 magnification subfields which were then stitched to obtain a complete image of the ventral, middle, and dorsal heads of the deltoid. Images were visualized using fluorescent microscopy (neurofilament conjugated to 488 nm and neuromuscular junctions conjugated to 647 nm). AChR were counted in ImageJ[62] using the multipoint tool. Muscle area was collected by opening the file in Dragonfly software (Object Research Systems, Montreal, Quebec, Canada) and separated by color channel. Muscle regions of interest were selected, and area measured based on autofluorescence in GFP channel.

4.10 | Micro-computed tomography

Micro-computed tomography (microCT) was used to obtain three-dimensional renderings of the left humerus of 8-week-old mice (n = 4 WT, n = 4 $Fgf9^{cKO}$) to visualize topographical data on DT volume, LSR volume, DT bone volume/ total volume (BV/TV), humerus diaphysis length. MicroCT scans were performed using a Scanco μCT 35 (X-ray energy: 60 kV; X-ray intensity: 95 mA; integration time: 1100 ms; voxel size: 10.6 μm; rotation step: 0.4°).[69] All raw scans were reconstructed and analyzed using Dragonfly software (Object Research Systems, Montreal, Quebec, Canada). Scans were aligned down the humeral axis and a box form was created to extract the bone ridges of interest. Using the spit at OTSU function, bone volume was selected based on voxel value. The bone analysis function was then used to fill in the bone volume and give the total volume. Diaphysis length was measured from the proximal growth plate to the Coronoid Fossa. After scans were obtained, humeri were decalcified in 14% EDTA, processed for paraffin embedding, sectioned at 7 μm thick, and stained with H&E. One $Fgf9^{cKO}$ sample and one WT sample were omitted due to processing errors.

4.11 | Neural/muscle-related gene expression

$Fgf9^{cKO}$ and WT littermates were aged to 3 weeks (n = 3 WT, n = 3 $Fgf9^{cKO}$) and 8 weeks of age (n = 4 WT, n = 3 $Fgf9^{cKO}$). qRT-PCR was used to compare differential gene expression of skeletal muscle using muscle contractility genes (*Dmpk*, *Mef2c*, and *Ikbkb*) and neural genes (*Nes*, *Agrn*, *Gap43*, *Ache*, *Rapsn*, *Chrne*, and *Musk*). Neural genes were selected for their role in the development and stabilization of neurons and neuromuscular junctions as well as for their role in the signal propagation and firing pathway. Contractility genes were chosen for their role in encoding genes necessary for cell-cell communication and differentiation, skeletal muscle contraction and relaxation, myogenesis, and homeostasis.[70] qRT-PCR, samples were amplified in triplicate and averaged together to calculate and ΔCT values with the average ΔCT of *ipo8* and *Rn18s* serving as the reference gene value. ΔCT values were converted to log-scale (log2ΔCT). Log scale was then presented as mean ± SD.

4.12 | Statistical analysis

Statistical analyses were performed in Prism (Prism GraphPad 6.0, LaJolla, California). For whole-mount area measurements, DT area was divided by the humerus area. For relative DT placement, distal length was divided by the whole length across the mineralized and whole humerus. The resulting ratios were compared through separate two-sample *t* tests. Hypertrophic cell area

measurements were averaged together per mouse and a two-sample *t* test compared the number of hypertrophic chondrocytes and the average hypertrophic chondrocyte area between $Fgf9^{null}$ embryos and WT embryos. A two-way ANOVA was run to compare cell density, proliferating cell density, and percent of proliferating cells for the EdU proliferation assay. The two-way ANOVA looked for differences between WT and $Fgf9^{null}$ embryos in the perichondrium, tendon, and deltoid-tendon attachment. Whole-mount, hypertrophic cell, and EdU quantifications were repeated by a separate observer through coded files to minimize bias. Two-way ANOVA was used to compare the osteoclast number between WT and $Fgf9^{null}$ samples at E16.5 and P0. For dynamic bone histomorphometry, three slides per sample were measured, and mineral growth rate was calculated. Technical replicates were averaged together per sample, and a two-sample *t* test was performed. A two-sample *t* test was used to compare $Fgf9^{cKO}$ gene expression. A two-sample *t* test was used to analyze LSR volume, DT volume, DT BV/TV, and humeri length between $Fgf9^{cKO}$ and WT mice at 8 weeks. Two-way ANOVA was used to compare gene expression and AchR clustering between $Fgf9^{cKO}$ and WT mice at 3 and 8-week time points.

ACKNOWLEDGMENTS

We thank Brewster Kingham, Summer Thompson, and Mark Shaw in the University of Delaware DNA Sequencing & Genotyping Center for assistance with for assistance with RNA sequencing; Shaneaka Anderson, Kierstyn Hendricks, and Kayleigh Denner for help with histology; Crystal Idleburg (Washington University) for TRAP staining; Karol Miaskiewicz for high performance computing support.

AUTHOR CONTRIBUTIONS

Connor Leek: Conceptualization; data curation; formal analysis; investigation; methodology; visualization; writing-original draft; writing-review & editing. **Jaclyn Soulas:** Conceptualization; data curation; formal analysis; investigation; methodology; visualization; writing-original draft; writing-review & editing. **Iman Bhattacharya:** Data curation; formal analysis; methodology; visualization; writing-original draft; writing-review & editing. **Elahe Ganji:** Data curation; formal analysis; investigation; methodology; visualization; writing-original draft; writing-review & editing. **Megan Smith:** Data curation; investigation; methodology; visualization; writing-original draft; writing-review & editing. **Ryan Locke:** Data curation; funding acquisition; methodology; writing-original draft; writing-review & editing. **Jaysheel Bhavsar:** Data curation; formal analysis; software; writing-original draft; writing-review & editing. **Shawn Polson:** Data curation; project administration; software; supervision; writing-original draft; writing-review & editing. **David Ornitz:** Conceptualization; funding acquisition; methodology; writing-original draft; writing-review & editing. **Megan Killian:** Conceptualization; data curation; formal analysis; funding acquisition; investigation; methodology; project administration; resources; software; supervision; validation; visualization; writing-original draft; writing-review & editing.

ORCID

Ryan C. Locke https://orcid.org/0000-0002-8466-3922
Shawn W. Polson https://orcid.org/0000-0002-3398-6932
David M. Ornitz https://orcid.org/0000-0003-1592-7629
Megan L. Killian https://orcid.org/0000-0001-6868-5550

REFERENCES

1. Kahn J, Shwartz Y, Blitz E, et al. Muscle contraction is necessary to maintain joint progenitor cell fate. *Dev Cell*. 2009;16(5):734-743. https://doi.org/10.1016/j.devcel.2009.04.013.
2. Arvind V, Huang AH. Mechanobiology of limb musculoskeletal development. *Ann N Y Acad Sci*. 2017;1409(1):18-32. https://doi.org/10.1111/nyas.13427.
3. Rot-Nikcevic I, Reddy T, Downing KJ, et al. Myf5−/−:MyoD−/− amyogenic fetuses reveal the importance of early contraction and static loading by striated muscle in mouse skeletogenesis. *Dev Genes Evol*. 2006;216(1):1-9. https://doi.org/10.1007/s00427-005-0024-9.
4. Blitz E, Viukov S, Sharir A, et al. Bone ridge patterning during musculoskeletal assembly is mediated through SCX regulation of Bmp4 at the tendon-skeleton junction. *Dev Cell*. 2009;17(6):861-873. https://doi.org/10.1016/j.devcel.2009.10.010.
5. Biewener AA, Fazzalari NL, Konieczynski DD, Baudinette RV. Adaptive changes in trabecular architecture in relation to functional strain patterns and disuse. *Bone*. 1996;19(1):1-8. https://doi.org/10.1016/8756-3282(96)00116-0.
6. Benjamin M, Toumi H, Ralphs JR, Bydder G, Best TM, Milz S. Where tendons and ligaments meet bone: attachment sites ('entheses') in relation to exercise and/or mechanical load. *J Anat*. 2006;208(4):471-490. https://doi.org/10.1111/j.1469-7580.2006.00540.x.
7. Blitz E, Sharir A, Akiyama H, Zelzer E. Tendon-bone attachment unit is formed modularly by a distinct pool of Scx- and Sox9-positive progenitors. *Development*. 2013;140(13):2680-2690. https://doi.org/10.1242/dev.093906.
8. Zelzer E, Blitz E, Killian ML, Thomopoulos S. Tendon-to-bone attachment: from development to maturity. *Birth Defects Res C Embryo Today*. 2014;102(1):101-112. https://doi.org/10.1002/bdrc.21056.
9. Tremblay P, Dietrich S, Mericskay M, Schubert FR, Li Z, Paulin D. A crucial role for Pax3 in the development of the hypaxial musculature and the long-range migration of muscle precursors. *Dev Biol*. 1998;203(1):49-61. https://doi.org/10.1006/dbio.1998.9041.

10. Pai AC. Developmental genetics of a lethal mutation, muscular dysgenesis (mdg), in the mouse. *Dev Biol*. 1965;11(1):82-92. https://doi.org/10.1016/0012-1606(65)90038-2.
11. Hamburger V, Waugh M. The primary development of the skeleton in nerveless and poorly innervated limb transplants of Chick embryos. *Physiol Zool*. 1940;13(4):367-382. https://doi.org/10.1086/physzool.13.4.30151585.
12. Felsenthal N, Rubin S, Stern T, et al. Development of migrating tendon-bone attachments involves replacement of progenitor populations. *Development*. 2018;145(24):dev165381. https://doi.org/10.1242/dev.165381.
13. Schwartz AG, Long F, Thomopoulos S, et al. Enthesis fibrocartilage cells originate from a population of hedgehog-responsive cells modulated by the loading environment. *Development*. 2015;142(1):196-206. https://doi.org/10.1242/dev.112714.
14. Hamrick MW, McPherron AC, Lovejoy CO. Bone mineral content and density in the Humerus of adult Myostatin-deficient mice. *Calcif Tissue Int*. 2002;71(1):63-68. https://doi.org/10.1007/s00223-001-1109-8.
15. Hung IH, Yu H, Lavine KJ, Ornitz DM. FGF9 regulates early hypertrophic chondrocyte differentiation and skeletal vascularization in the developing stylopod. *Dev Biol*. 2007;307(2):300-313. https://doi.org/10.1016/j.ydbio.2007.04.048.
16. Hung IH, Schoenwolf GC, Lewandoski M, Ornitz DM. A combined series of Fgf9 and Fgf18 mutant alleles identifies unique and redundant roles in skeletal development. *Dev Biol*. 2016;411(1):72-84. https://doi.org/10.1016/j.ydbio.2016.01.008.
17. Ornitz DM, Marie PJ. Fibroblast growth factor signaling in skeletal development and disease. *Genes Dev*. 2015;29(14):1463-1486. https://doi.org/10.1101/gad.266551.115.
18. Ornitz DM, Itoh N. The fibroblast growth factor signaling pathway. *Wiley Interdiscip Rev Dev Biol*. 2015;4(3):215-266. https://doi.org/10.1002/wdev.176.
19. Berendsen AD, Olsen BR. Bone development. *Bone*. 2015;80:14-18. https://doi.org/10.1016/j.bone.2015.04.035.
20. Su N, Jin M, Chen L. Role of FGF/FGFR signaling in skeletal development and homeostasis: learning from mouse models. *Bone Res*. 2014;2:14003. https://doi.org/10.1038/boneres.2014.3.
21. Ornitz DM, Marie PJ. FGF signaling pathways in endochondral and intramembranous bone development and human genetic disease. *Genes Dev*. 2002;16(12):1446-1465. https://doi.org/10.1101/gad.990702.
22. Sahni M, Ambrosetti DC, Mansukhani A, Gertner R, Levy D, Basilico C. FGF signaling inhibits chondrocyte proliferation and regulates bone development through the STAT-1 pathway. *Genes Dev*. 1999;13(11):1361-1366. https://doi.org/10.1101/gad.13.11.1361.
23. Deng C, Wynshaw-Boris A, Zhou F, Kuo A, Leder P. Fibroblast growth factor receptor 3 is a negative regulator of bone growth. *Cell*. 1996;84(6):911-921. https://doi.org/10.1016/s0092-8674(00)81069-7.
24. Coutu DL, François M, Galipeau J. Inhibition of cellular senescence by developmentally regulated FGF receptors in mesenchymal stem cells. *Blood*. 2011;117(25):6801-6812. https://doi.org/10.1182/blood-2010-12-321539.
25. Jacob AL, Smith C, Partanen J, Ornitz DM. Fibroblast growth factor receptor 1 signaling in the osteo-chondrogenic cell lineage regulates sequential steps of osteoblast maturation. *Dev Biol*. 2006;296(2):315-328. https://doi.org/10.1016/j.ydbio.2006.05.031.
26. Karuppaiah K, Yu K, Lim J, et al. FGF signaling in the osteoprogenitor lineage non-autonomously regulates postnatal chondrocyte proliferation and skeletal growth. *Development*. 2016;143(10):1811-1822. https://doi.org/10.1242/dev.131722.
27. Vaahtokari A, Aberg T, Thesleff I. Apoptosis in the developing tooth: association with an embryonic signaling center and suppression by EGF and FGF-4. *Development*. 1996;122(1):121-129.
28. Ohbayashi N, Shibayama M, Kurotaki Y, et al. FGF18 is required for normal cell proliferation and differentiation during osteogenesis and chondrogenesis. *Genes Dev*. 2002;16(7):870-879. https://doi.org/10.1101/gad.965702.
29. Colvin JS, Feldman B, Nadeau JH, Goldfarb M, Ornitz DM. Genomic organization and embryonic expression of the mouse fibroblast growth factor 9 gene. *Dev Dyn*. 1999;216(1):72-88. https://doi.org/10.1002/(SICI)1097-0177(199909)216:1<72::AID-DVDY9>3.0.CO;2-9.
30. Garofalo S, Kliger-Spatz M, Cooke JL, et al. Skeletal dysplasia and defective chondrocyte differentiation by targeted overexpression of fibroblast growth factor 9 in transgenic mice. *J Bone Miner Res*. 1999;14(11):1909-1915. https://doi.org/10.1359/jbmr.1999.14.11.1909.
31. Yang Y, Kozin SH. Cell signaling regulation of vertebrate limb growth and patterning. *J Bone Joint Surg Am*. 2009;91(Suppl 4):76-80. https://doi.org/10.2106/JBJS.I.00079.
32. Govindarajan V, Overbeek PA. FGF9 can induce endochondral ossification in cranial mesenchyme. *BMC Dev Biol*. 2006;6:7. https://doi.org/10.1186/1471-213X-6-7.
33. Lu J, Dai J, Wang X, et al. Effect of fibroblast growth factor 9 on the osteogenic differentiation of bone marrow stromal stem cells and dental pulp stem cells. *Mol Med Rep*. 2015;11(3):1661-1668. https://doi.org/10.3892/mmr.2014.2998.
34. Huang DW, Sherman BT, Lempicki RA. Bioinformatics enrichment tools: paths toward the comprehensive functional analysis of large gene lists. *Nucleic Acids Res*. 2009;37(1):1-13. https://doi.org/10.1093/nar/gkn923.
35. Huang DW, Sherman BT, Lempicki RA. Systematic and integrative analysis of large gene lists using DAVID bioinformatics resources. *Nat Protoc*. 2009;4(1):44-57. https://doi.org/10.1038/nprot.2008.211.
36. Pan Y, Bai CB, Joyner AL, Wang B. Sonic hedgehog Signaling regulates Gli2 transcriptional activity by suppressing its processing and degradation. *Mol Cell Biol*. 2006;26(9):3365-3377. https://doi.org/10.1128/MCB.26.9.3365-3377.2006.
37. Tan Z, Niu B, Tsang KY, et al. Synergistic co-regulation and competition by a SOX9-GLI-FOXA phasic transcriptional network coordinate chondrocyte differentiation transitions. Barsh GS, ed. *PLoS Genet*. 2018;14(4):e1007346. https://doi.org/10.1371/journal.pgen.1007346.
38. Akiyama H. The transcription factor Sox9 has essential roles in successive steps of the chondrocyte differentiation pathway and is required for expression of Sox5 and Sox6. *Genes Dev*. 2002;16(21):2813-2828. https://doi.org/10.1101/gad.1017802.
39. Long F. Ihh signaling is directly required for the osteoblast lineage in the endochondral skeleton. *Development*. 2004;131(6):1309-1318. https://doi.org/10.1242/dev.01006.
40. Mau E, Whetstone H, Yu C, Hopyan S, Wunder JS, Alman BA. PTHrP regulates growth plate chondrocyte differentiation and

proliferation in a Gli3 dependent manner utilizing hedgehog ligand dependent and independent mechanisms. *Dev Biol*. 2007;305(1):28-39. https://doi.org/10.1016/j.ydbio.2007.01.031.
41. St-Jacques B, Hammerschmidt M, McMahon AP. Indian hedgehog signaling regulates proliferation and differentiation of chondrocytes and is essential for bone formation. *Genes Dev*. 1999;13(16):2072-2086. https://doi.org/10.1101/gad.13.16.2072.
42. Leung VYL, Gao B, Leung KKH, et al. SOX9 governs differentiation stage-specific gene expression in growth plate chondrocytes via direct concomitant transactivation and Repression. Van Heyningen V, ed. *PLoS Genet*. 2011;7(11): e1002356. https://doi.org/10.1371/journal.pgen.1002356.
43. Lanske B, Karaplis AC, Lee K, et al. PTH/PTHrP receptor in early development and Indian hedgehog- -regulated bone growth. *Science*. 1996;273(5275):663-666. https://doi.org/10.1126/science.273.5275.663.
44. Winkler DG, Sutherland MK, Geoghegan JC, et al. Osteocyte control of bone formation via sclerostin, a novel BMP antagonist. *EMBO J*. 2003;22(23):6267-6276. https://doi.org/10.1093/emboj/cdg599.
45. Peters KG, Werner S, Chen G, Williams LT. Two FGF receptor genes are differentially expressed in epithelial and mesenchymal tissues during limb formation and organogenesis in the mouse. *Development*. 1992;114(1):233-243.
46. Henderson JE, Naski MC, Aarts MM, et al. Expression of FGFR3 with the G380R achondroplasia mutation inhibits proliferation and maturation of CFK2 Chondrocytic cells. *J Bone Miner Res*. 2000;15(1):155-165. https://doi.org/10.1359/jbmr.2000.15.1.155.
47. Roberts RR, Bobzin L, Teng CS, et al. FGF signaling patterns cell fate at the interface between tendon and bone. *Development*. 2019;146(15):dev170241. https://doi.org/10.1242/dev.170241.
48. Eyal S, Kult S, Rubin S, et al. Bone morphology is regulated modularly by global and regional genetic programs. *Development*. 2019;146(14):dev167882. https://doi.org/10.1242/dev.167882.
49. Cooper KL, Oh S, Sung Y, Dasari RR, Kirschner MW, Tabin CJ. Multiple phases of chondrocyte enlargement underlie differences in skeletal proportions. *Nature*. 2013;495(7441): 375-378. https://doi.org/10.1038/nature11940.
50. Sears KE, Behringer RR, Rasweiler JJ, Niswander LA. Development of bat flight: morphologic and molecular evolution of bat wing digits. *Proc Natl Acad Sci U S A*. 2006;103(17):6581-6586. https://doi.org/10.1073/pnas.0509716103.
51. Cooper KL. The lesser Egyptian jerboa, *Jaculus jaculus*: a unique rodent model for evolution and development. *Cold Spring Harb Protoc*. 2011;2011(12):1451-1456. https://doi.org/10.1101/pdb.emo066704.
52. Galea GL, Zein MR, Allen S, Francis-West P. Making and shaping endochondral and intramembranous bones. *Dev Dyn*. 2021; 250(3):414-449. https://doi.org/10.1002/dvdy.278.
53. Huang J, Wang K, Shiflett LA, et al. Fibroblast growth factor 9 (FGF9) inhibits myogenic differentiation of C2C12 and human muscle cells. *Cell Cycle*. 2019;18(24):3562-3580. https://doi.org/10.1080/15384101.2019.1691796.
54. Girgenrath S, Song K, Whittemore L-A. Loss of myostatin expression alters fiber-type distribution and expression of myosin heavy chain isoforms in slow- and fast-type skeletal muscle. *Muscle Nerve*. 2005;31(1):34-40. https://doi.org/10.1002/mus.20175.
55. Hennebry A, Berry C, Siriett V, et al. Myostatin regulates fiber-type composition of skeletal muscle by regulating MEF2 and MyoD gene expression. *Am J Physiol Cell Physiol*. 2009;296(3): C525-C534. https://doi.org/10.1152/ajpcell.00259.2007.
56. Elkasrawy MN, Hamrick MW. Myostatin (GDF-8) as a key factor linking muscle mass and bone structure. *J Musculoskelet Neuronal Interact*. 2010;10(1):56-63. https://doi.org/10.1016/j.biotechadv.2011.08.021.Secreted.
57. Solem RC, Eames BF, Tokita M, Schneider RA. Mesenchymal and mechanical mechanisms of secondary cartilage induction. *Dev Biol*. 2011;356(1):28-39. https://doi.org/10.1016/j.ydbio.2011.05.003.
58. Newman RA, Sorensen BR, Kilpatrick AM, Shea MA. Calcium-dependent energetics of calmodulin domain interactions with regulatory regions of the ryanodine receptor type 1 (RyR1). *Biophys Chem*. 2014;193-194:35-49. https://doi.org/10.1016/j.bpc.2014.07.004.
59. Nishizawa Y, Okui Y, Inaba M, et al. Calcium/calmodulin-mediated action of calcitonin on lipid metabolism in rats. *J Clin Invest*. 1988;82(4):1165-1172. https://doi.org/10.1172/JCI113713.
60. Colvin JS, White AC, Pratt SJ, Ornitz DM. Lung hypoplasia and neonatal death in Fgf9-null mice identify this gene as an essential regulator of lung mesenchyme. *Development*. 2001;128 (11):2095-2106.
61. Rigueur D, Lyons KM. Whole-mount skeletal staining. *Methods Mol Biol*. 2014;1130:113-121. https://doi.org/10.1007/978-1-62703-989-5_9.
62. Schneider CA, Rasband WS, Eliceiri KW. NIH image to ImageJ: 25 years of image analysis. *Nat Methods*. 2012;9(7):671-675. https://doi.org/10.1038/nmeth.2089.
63. Kim D, Pertea G, Trapnell C, Pimentel H, Kelley R, Salzberg SL. TopHat2: accurate alignment of transcriptomes in the presence of insertions, deletions and gene fusions. *Genome Biol*. 2013;14(4):R36. https://doi.org/10.1186/gb-2013-14-4-r36.
64. Wang L, Wang S, Li W. RSeQC: quality control of RNA-seq experiments. *Bioinformatics*. 2012;28(16):2184-2185. https://doi.org/10.1093/bioinformatics/bts356.
65. Anders S, Pyl PT, Huber W. HTSeq- -a python framework to work with high-throughput sequencing data. *Bioinformatics*. 2015;31(2):166-169. https://doi.org/10.1093/bioinformatics/btu638.
66. Robinson MD, McCarthy DJ, Smyth GK. edgeR: a Bioconductor package for differential expression analysis of digital gene expression data. *Bioinformatics*. 2010;26(1):139-140. https://doi.org/10.1093/bioinformatics/btp616.
67. Benjamini Y, Hochberg Y. Controlling the false discovery rate: a practical and powerful approach to multiple testing. *J R Stat Soc B Methodol*. 1995;57(1):289-300. https://doi.org/10.1111/j.2517-6161.1995.tb02031.x.
68. Mead RJ, Bennett EJ, Kennerley AJ, et al. Optimised and rapid pre-clinical screening in the SOD1G93A transgenic mouse model of amyotrophic lateral sclerosis (ALS). *PLoS One*. 2011;6 (8):e23244. https://doi.org/10.1371/journal.pone.0023244.

69. Bouxsein ML, Boyd SK, Christiansen BA, Guldberg RE, Jepsen KJ, Müller R. Guidelines for assessment of bone microstructure in rodents using micro-computed tomography. *J Bone Miner Res*. 2010;25(7):1468-1486. https://doi.org/10.1002/jbmr.141.
70. Bakkar N, Wang J, Ladner KJ, et al. IKK/NF-κB regulates skeletal myogenesis via a signaling switch to inhibit differentiation and promote mitochondrial biogenesis. *J Cell Biol*. 2008;180(4):787-802. https://doi.org/10.1083/jcb.200707179.

How to cite this article: Leek CC, Soulas JM, Bhattacharya I, et al. Deletion of *Fibroblast growth factor 9* globally and in skeletal muscle results in enlarged tuberosities at sites of deltoid tendon attachments. *Developmental Dynamics*. 2021;250(12):1778–1795. https://doi.org/10.1002/dvdy.383